




Diffusive skin effect and topological heat funneling

Pei-Chao Cao^{1,4}, Ying Li ^{2,3,4}✉, Yu-Gui Peng ¹, Minghong Qi^{2,3}, Wen-Xi Huang¹, Peng-Qi Li¹ & Xue-Feng Zhu ¹✉

Non-Hermitian wave system has attracted intense attentions in the past decade since it reveals interesting physics and generates various counterintuitive effects. However, in the diffusive system that is inherently non-Hermitian with natural dissipation, the robust control of heat flow is hitherto still a challenge. Here we introduce the skin effect into diffusive systems. Different from the skin effect in wave systems, where asymmetric couplings were enabled by dynamic modulations or judicious gain/loss engineering, asymmetric couplings of the temperature fields in diffusive systems can be realized by directly contacted metamaterial channels. Topological heat funneling is further presented, where the temperature field automatically concentrates towards a designated position and shows a strong immunity against the defects. Our work indicates that the diffusive system can provide a distinctive platform for exploring non-Hermitian physics as well as thermal topology.

¹School of Physics and Innovation Institute, Huazhong University of Science and Technology, Wuhan 430074, China. ²Interdisciplinary Center for Quantum Information, State Key Laboratory of Modern Optical Instrumentation, ZJU-Hangzhou Global Scientific and Technological Innovation Center, Zhejiang University, Hangzhou 310027, China. ³International Joint Innovation Center, Key Lab. of Advanced Micro/Nano Electronic Devices & Smart Systems of Zhejiang, The Electromagnetics Academy at Zhejiang University, Zhejiang University, Haining 314400, China. ⁴These authors contributed equally: Pei-Chao Cao, Ying Li. ✉email: eleying@zju.edu.cn; xfzhu@hust.edu.cn

Non-Hermitian Hamiltonian plays a core role to describe systems that exchange energy with the environment. In wave systems, the non-Hermitian physics has been explored intensely in the past decade^{1–5}. For example, the parity-time symmetric system that operates at an exceptional point (EP) can realize unidirectionally invisible cloak⁶, single mode laser⁷, one-way mode switcher^{8,9}, high-sensitivity sensor¹⁰, and wireless power transfer^{11,12}. The dynamically modulated systems with a broken time-reversal symmetry can produce various novel gyrators, isolators and circulators¹³. Besides, an intriguing “skin effect” was recently discovered in non-Hermitian systems, where all the bulk states localize at the edges under the open boundary condition (OBC), which modifies the bulk-boundary correspondence in Hermitian cases^{14–22}. The non-Hermitian skin effect shows application prospects in the nonreciprocal energy manipulation and has been demonstrated in various fields such as optical lattices²³, mechanical systems²⁴, quantum-walk networks²⁵, and electrical circuits²⁶, etc.

In diffusive systems that are non-Hermitian inherently, the thermal metamaterials advanced rapidly as it enables various agile and flexible manipulation of heat flow^{27,28}. Based on the theory of transformation thermotics, fruitful progresses have been achieved, such as thermal cloaks that conceal objects in heat conduction or radiative camouflages against infrared detection^{29–31}, thermal diodes and concentrators that isolate and harvest heat directionally^{32–35}. Since the diffusive system is dissipative, it provides a natural platform to investigate the non-Hermitian physics, for example, the observation of anti-parity-time symmetric phase transition at an EP^{36–38}. The Hamiltonian respecting anti-parity-time symmetry can be constructed by imposing the convection to diffusive systems, which generates dynamically “stopped” temperature fields³⁶. However, the diffusive counterparts of asymmetric coupling and skin effect have not been discovered hitherto. Due to the symmetric energy exchanges in general cases, breaking the time-reversal symmetry with temporal modulations²³ and judicious gain/loss engineering of couplings²⁶ were considered the few-in-number choices.

In this work, we show that it is possible to realize asymmetric coupling and skin effect in the diffusive systems by directly contacting thermal metamaterials. Different from the cases in

wave systems, the effective non-Hermitian Hamiltonians describing asymmetric couplings in diffusive systems are imaginary due to the dissipative nature, as shown in Fig. 1a. Our finding starts from the fact that heat and temperature variations during the energy exchange are not equivalent. Temperature evolution is actually asymmetric between different components. As a result, we realize the diffusive skin effect, which shows that the eigenstates in all bulk bands can become localized edge states under open boundaries. This is fundamentally different from the Hermitian case in which only the edge modes can have boundary localizations. Unlike the non-Hermitian skin effects in the wave systems, where the asymmetric couplings were implemented by temporal modulations or tailored gain/loss couplings, asymmetric coupling of temperature fields can be easily enabled by the directly contacted thermal metamaterials. We further propose an approach to construct a periodic non-Hermitian Hamiltonian in the parameter space from an aperiodic structure. On this basis, the skin-effect-induced heat funneling is showcased, where temperature fields concentrate to the designated position, being regardless of the initial condition and showing a strong immunity against the defects, as schematically shown in Fig. 1b. The robust temperature fields with nontrivial gradients can be useful for thermoelectric power generation or heat harvesting³⁹. Moreover, the high sensitivity of diffusive skin effect to the change of boundary conditions makes it possible to achieve topological thermal sensing⁴⁰.

Results

Directly asymmetric coupling. In order to understand the asymmetric coupling diffusive systems intuitively, we can start from a double-ring toy model that was experimentally demonstrated recently³⁶. As shown in Fig. 2a, where two rings are vertically coupled in z direction through an interlayer. According to the Fourier’s law in heat conduction, the coupling equations can be written as^{36–38}

$$\begin{aligned} \frac{\partial T_1}{\partial t} &= D_1 \frac{\partial^2 T_1}{\partial x^2} + h_{21}(T_2 - T_1), \\ \frac{\partial T_2}{\partial t} &= D_2 \frac{\partial^2 T_2}{\partial x^2} + h_{12}(T_1 - T_2), \end{aligned} \quad (1)$$

where T_1 (T_2) is the temperature field of upper (lower) channel and $D_1 = \frac{\kappa_1}{\rho_1 C_1}$ ($D_2 = \frac{\kappa_2}{\rho_2 C_2}$) is the diffusivity of the upper (lower)

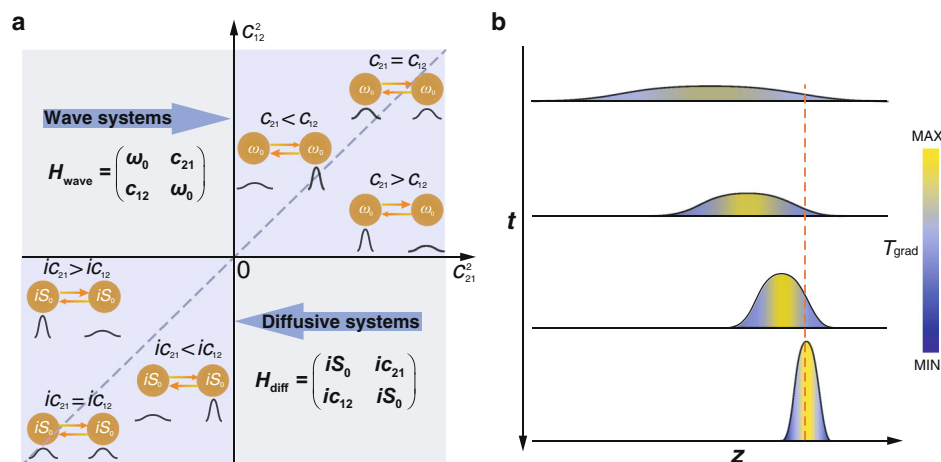


Fig. 1 Asymmetric coupling and heat funneling. **a** Schematic of coupling dynamics with Hamiltonians in the wave and diffusive systems. The main diagonal elements are the decoupled on-site resonant frequency (ω_0) in wave systems and the decay rate (iS_0) in diffusive systems, the off-diagonal elements are the coupling coefficients ($c_{12,21}$ and $ic_{12,21}$). Elements in the diffusive systems are imaginary, indicating the dissipative nature of heat transfer. The black curves describe the field distributions for symmetric and asymmetric couplings. **b** Concept of the heat funneling effect, showing that the temperature field is rapidly gathered at where we specify (the dashed red line), and finally achieve a steady state. t axis indicates the time evolution and z axis is along the coupling direction.

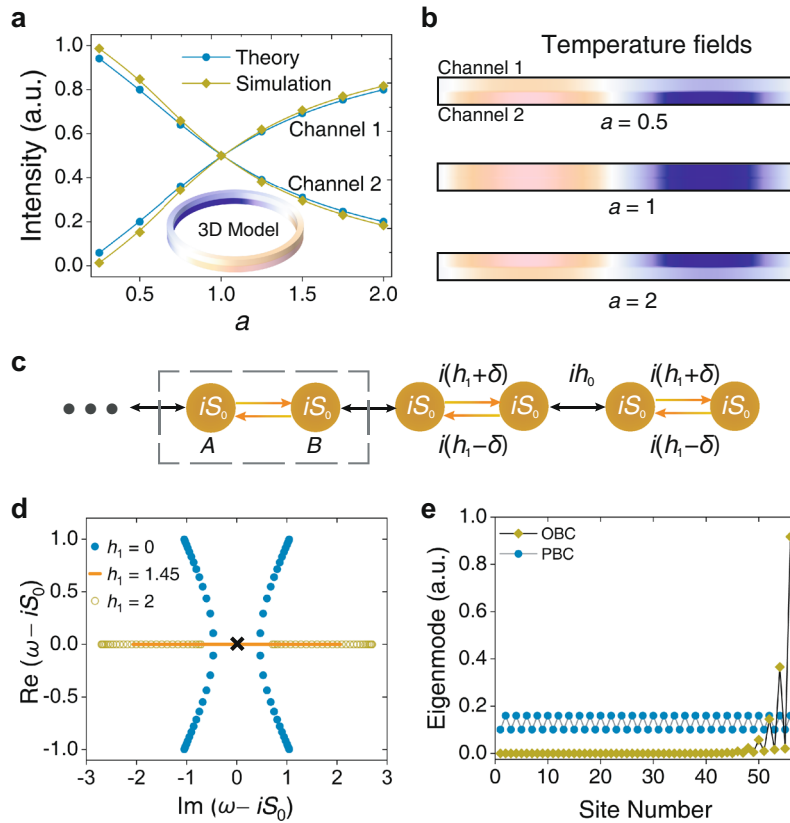


Fig. 2 Asymmetric coupling model and diffusive skin effect. **a, b** Temperature fields intensities and distributions of two directly coupled channels versus the asymmetric factor a . Note that at $a = 1$, the temperature field distribution is symmetric, the insert shows the 3D model at $a = 0.5$. **c** The diffusive tight-binding Su-Schrieffer-Heeger (SSH) model for open boundary condition (OBC) with asymmetric intracell coupling $i(h_1 \pm \delta)$ and symmetric intercell coupling ih_0 , iS_0 is the unified decay rate on each site. **d** Spectra in the complex plane at coupling parameters $h_1 = 0, 1.45, 2$ for OBC with $h_0 = 1$ and $\delta = 1.05$. **e** Amplitude distributions of eigenstates for OBC and periodic boundary condition (PBC), at $h_1 = 1.45$. The unitcell number is 28.

channel with κ_1 (κ_2), ρ_1 (ρ_2) and C_1 (C_2) being the thermal conductivity, mass density and heat capacity. x is the position along the channel. The heat exchange rate of the upper (lower) channel is $h_{21} = \frac{\kappa_1}{\rho_1 C_1 b d}$ ($h_{12} = \frac{\kappa_2}{\rho_2 C_2 b d}$), where κ_i is the thermal conductivity of the coupling layer, b and d are the thicknesses of the ring channel.

As the temperature field in the ring structure is spatially periodic, we can assume that Eq. (1) has a wave-like solution of $T_{1,2} = A_{1,2} e^{i(\beta x - \omega_{1,2} t)} + T_0$ ³⁶. In the solution, $A_{1,2}$ is the amplitude, β is the propagation constant, $\omega_{1,2}$ is the complex frequency, and T_0 is the reference temperature that is set to be zero for simplicity. Here we employ the temperature gradient and position of maximum temperature to represent the amplitude and phase of the wave-like solution. As all the ring channels have the same size, the propagating constants of circulating “heat wave” in them are equal to be $\beta = m \frac{2\pi}{2\pi R} = \frac{m}{R}$, where m is the mode order and R is the radius of the ring. Usually, only the first-order mode is taken into consideration, since it is very stable and can be selectively excited. Temperature variations in each channel can be regarded as uniform on condition that the layers are thin enough. As a result, the heat transfer in these channels possess coherent properties. Substituting the wave-like solution into Eq. (1) and considering the boundary continuity condition, we can deduce an effective Hamiltonian about (A_1, A_2) ^{T36-38}

$$H_0 = \begin{pmatrix} iS_1 & ih_{21} \\ ih_{12} & iS_2 \end{pmatrix}, \quad (2)$$

where $S_1 = -(\beta^2 D_1 + h_{21})$ and $S_2 = -(\beta^2 D_2 + h_{12})$. In Eq. (2), the Hamiltonian of the diffusive system is imaginary, which is different from the one in the wave system (real), as shown in Fig. 1a. Moreover, when the material parameters $\rho_1 C_1 \neq \rho_2 C_2$, the ring coupling becomes asymmetric with $ih_{21} \neq ih_{12}$. It needs to be pointed out that the main diagonal elements in Eq. (2) can be unified into iS_0 by adjusting the diffusivities $D_{1,2}$ along with $h_{21,12}$, where $ih_{21,12}$ are replaced by $ic_{21,12}$ in Fig. 1a. Eigenvalues and eigenvectors of Eq. (2) are solved to be $\omega_{\pm} = i(S_0 \pm \sqrt{h_{12} h_{21}})$ and $u_{\pm} = (A_{\pm 1}, A_{\pm 2})^T = e^{-i\omega_{\pm} t} \left(\pm \sqrt{\frac{h_{12}}{h_{21}}}, 1 \right)^T$. We can find the amplitudes in channels are asymmetric in the steady state, meanwhile, they are always time dependent with the factor of $e^{-i\omega_{\pm} t}$ due to the system is dissipative. Therefore, our structure does not require dynamic modulation or gain-loss engineering to achieve asymmetric couplings.

Diffusive skin effect and non-Bloch band theory. For implementation, we can take the densities of directly coupled channels varying with a ratio of a^2 . Figures 2a and 2b display the asymmetric coupling temperature fields with different a , respectively. In order to realize the non-Hermitian diffusive Su-Schrieffer-Heeger (SSH) model, we can connect the asymmetric coupling unit cells with symmetric couplings in Fig. 2c¹⁶. Each unit cell consists of sublattices (A+B), where the asymmetric intracell couplings and symmetric intercell coupling are $i(h_1 \pm \delta)$ and ih_0 , respectively. For the open boundary condition, the Hamiltonian

is^{16,20}

$$H_{\text{OBC}} = iS_0 \sum_l [\hat{A}_l^\dagger \hat{A}_l + \hat{B}_l^\dagger \hat{B}_l] + \sum_l [i(h_1 + \delta) \hat{B}_l^\dagger \hat{A}_l + i(h_1 - \delta) \hat{A}_l^\dagger \hat{B}_l + ih_0(\hat{B}_l^\dagger \hat{A}_{l+1} + \hat{A}_l^\dagger \hat{B}_{l-1})], \quad (3)$$

where \hat{A}_l^\dagger and \hat{B}_l^\dagger are the creation operators of A and B sites in the l th period. For the periodic boundary condition (PBC), the Bloch-mode Hamiltonian in momentum space is expressed into

$$H_{\text{PBC}}(K) = iS_0 \hat{I} + i(h_1 + h_0 \cos K) \hat{\sigma}_x + i(h_0 \sin K - i\delta) \hat{\sigma}_y, \quad (4)$$

which respects the sublattice symmetry of $\hat{\sigma}_z^{-1}(H_{\text{PBC}}(K) - iS_0 \hat{I}) \hat{\sigma}_z = -(H_{\text{PBC}}(K) - iS_0 \hat{I})$ with $\hat{\sigma}_{x,y,z}$ the Pauli matrices and K the Bloch vector¹⁹. Eigenvalues of Eq. (4) can be deduced

$$\omega_{\pm}(K) = iS_0 \pm i\sqrt{d_x^2 + (d_y - i\delta)^2}, \quad (5)$$

where $d_x = h_1 + h_0 \cos K$ and $d_y = h_0 \sin K$. When the complex spectrum at the zero-energy level, *viz.*, $\omega_{\pm}(K) - iS_0 = 0$, we can obtain EPs at which all eigenstates degenerate (the sign ‘ \times ’ in Fig. 2d). However, the EPs deduced from the PBC case ($h_1 = 2.05$) contradict the OBC one ($h_1 = 1.45$), which indicates the bulk boundary correspondence breaks down (the complex spectrum of PBC case can be found in Supplementary Note 1)^{16,20}. Back to the OBC case, where the eigen-equation $(H_{\text{OBC}} - iS_0 \hat{I})\Psi = (\omega - iS_0)\Psi$ with $\Psi = (T_{A,1}, T_{B,1}, \dots, T_{A,l}, T_{B,l}, \dots, T_{A,N}, T_{B,N})^T$, the non-Hermitian Bloch vector should be modified into complex to eliminate the influence of boundary condition. Here the generalized Bloch vector $K \rightarrow K - i \ln r$ ($r = \sqrt{\frac{h_1 + \delta}{h_1 - \delta}}$) and the Bloch phase

factor $e^{iK} \rightarrow \alpha = re^{iK}$ ^{16,20}. According to the non-Bloch band theory, the nearest neighbor coupling of temperature fields can be further transformed into

$$\begin{aligned} i[(h_1 + \delta) + h_0 \alpha] \phi_A &= (\omega_l - iS_0) \phi_B, \\ i[(h_1 - \delta) + h_0 / \alpha] \phi_B &= (\omega_l - iS_0) \phi_A, \end{aligned} \quad (6)$$

where $\phi_{A,B} = \alpha^l \phi_{A_l, B_l}$ are the eigenstates in l th unit cell and degenerate at $\omega_l - iS_0 = 0$ (also at the EPs) with the generalized phase factor

$$|\alpha_{\pm}| = \left| \frac{h_1 + \delta}{h_0} \right|, \left| \frac{h_0}{h_1 - \delta} \right|. \quad (7)$$

Therefore, EPs locate at the hyperbolic curve $|\frac{h_1}{h_0}|^2 - (\frac{\delta}{h_0})^2 = 1$. The corresponding amplitudes of eigenstates for PBC and OBC at the EP are shown in Fig. 2e and Fig. S2 (in Supplementary Note 2). Here the EP is also a topological phase transition point and the topological phase diagram is shown in the ‘‘Methods’’.

Heat funneling effect. Figure 3a presents the heat funnel model with two mirrored SSH chains splicing at the designated interface. In our case, there are 5 periods for the left chain and 1 period for the right chain. The thicknesses of ring channels and interlayers are b and d . The internal and external radii of each channel are R_1 and R_2 with $R_1 \approx R_2$. We define the propagation constant of temperature fields as $\beta = \frac{1}{R_1}$. The thermal conductivities, mass densities and capacities of thermal metamaterials for ring channels and coupling interlayers are (κ_n, ρ_n, C_0) and $(\kappa_{in}, \rho_0, C_0)$, where the channel number n indicates that the associated material parameters are varied.

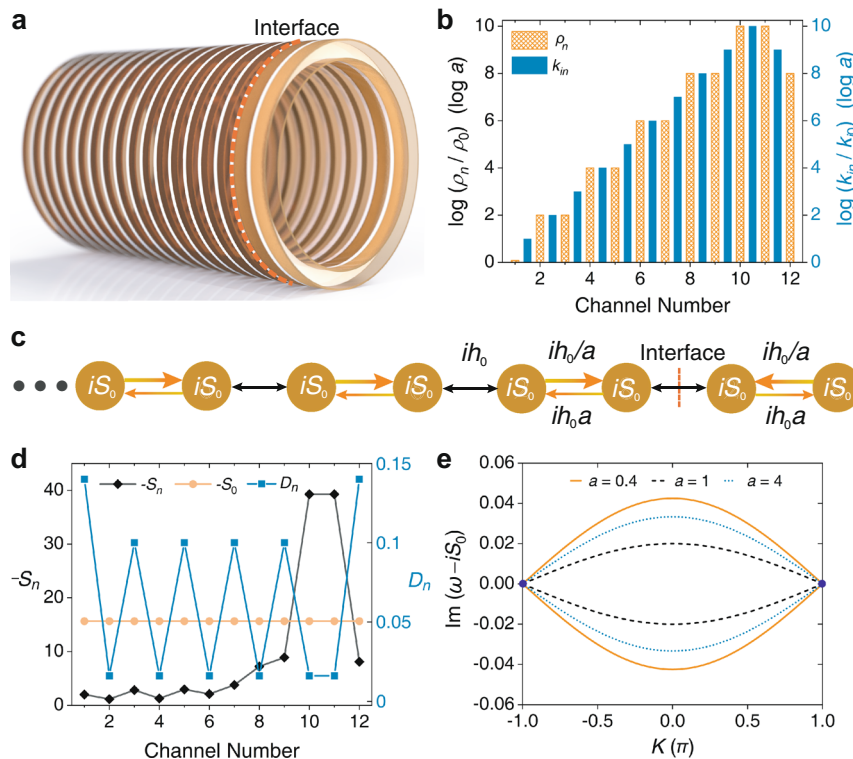


Fig. 3 Heat funneling model. **a** Schematic of the coupled ring structure for realization, where the red dashed line denotes the position of interface, there are 5 periods for the left chain and 1 period for the right chain. **b** Thermal conductivity (κ_n) and mass density (ρ_n) distributions of thermal metamaterials for the ring channels and coupling interlayers. **c** Equivalent tight-binding model, with the asymmetric intracell couplings are $\frac{ih_0}{a}$ and $ih_0 a$. **d** Homogenization of the decay rates of channels iS_n at $a = 0.4$, D_n are the diffusivity of channels. **e** Generalized gapless Bloch bands of the non-Hermitian Su-Schrieffer-Heeger (SSH) model at $a = 0.4, 1, 4$, K is Bloch vector and ω is the eigenfrequency.

The coupling coefficients between channels n and $n + 1$ can be expressed into $ih_{n,n+1} = i\frac{\kappa_{in}}{\rho_{n+1}C_0bd}$ and $ih_{n+1,n} = i\frac{\kappa_{in}}{\rho_n C_0bd}$ for the forward and backward couplings, respectively. In order to keep the couplings in the non-Hermitian diffusive SSH model respecting the translation symmetry in parameter spaces, the parameters ρ_n and κ_{in} of thermal metamaterials should be arranged as

$$\rho_n = \begin{cases} a^{n-1}\rho_0, & n = 1, 3, 5, \dots \\ a^n\rho_0, & n = 2, 4, 6, \dots \end{cases}, \quad \kappa_{in} = a^n\kappa_{i0}, \quad n = 1, 2, 3, 4, \dots, \quad (8)$$

which is shown by the setting of the heat funnel model in Fig. 3b. However, it is difficult to find the natural materials that satisfies these gradient parameters in implementation. According to the effective medium theory, we can realize the effective densities of channels and the effective thermal conductivities of coupling interlayers with composite metamaterials. In this way, the effective material parameters can be satisfied by modulating the doping rates of materials with highly contrasted properties (such as Cu and Polydimethylsiloxane). Here the asymmetric intracell couplings are $\frac{ih_0}{a}$ and ih_0a , with the symmetric intercell coupling ih_0 , where $h_0 = \frac{\kappa_0}{\rho_0 C_0 bd}$. From the semi-infinite model in Fig. 2c, we can easily obtain $h_1 = \frac{1}{2}h_0(\frac{1}{a} + a)$, $\delta = \frac{1}{2}h_0(\frac{1}{a} - a)$. However, this cannot lead to the equivalent tight-binding model in Fig. 3c, if the diffusivity takes the form of $D_n = \frac{\kappa_0}{\rho_n C_0}$ (the diamond dots in Fig. 3d). The eigenfrequency of $iS_n = -i(\beta^2 D_n + h_{n,n+1} + h_{n+1,n})$ should be uniformed. Here we adjust D_n in the way shown by the square dots in Fig. 3d to homogenize iS_n into $iS_0 = -i(\beta^2 D_0 + (a + \frac{1}{a} + 1)h_0)$ (the circular dots in Fig. 3d), with $D_0 = \frac{\kappa_0}{\rho_0 C_0}$. The Hamiltonian of non-Hermitian SSH model can be derived by replacing K with $K + i\ln a$ and the eigenvalues are deduced as $\omega_{\pm}(K) - iS_0 = \pm i2h_0 \cos \frac{K}{2}$. It is interesting to find that the system operates exactly at the topological transition point with a gapless band for any value of a . The generalized Bloch band is plotted in Fig. 3e, where the blue dots denote EPs.

We construct the 2D heat funnel model for simplicity in the theoretical analysis and the full wave simulations here. The structural parameters are chosen as $b = 5$ mm, $d = 1$ mm, and $R_1 \approx R_2 = 100$ mm. The material parameters are set to be $\rho_0 = 1000$ kg m⁻³, $C_0 = 1000$ J kg⁻¹K⁻¹, $\kappa_0 = 100$ W m⁻¹K⁻¹, and $\kappa_{i0} = 5$ W m⁻¹K⁻¹. In Figs. 4a, c, we show the imaginary eigenvalues $-\text{Im} \omega$ and the eigenmodes ($|\phi_n\rangle$) at $a = 1, 0.4$. The result reveals that the temperature gradients of all eigenmodes are almost evenly distributed in the channel array at $a = 1$. While at $a = 0.4$, the temperature fields will localize in the interface channels. For experiments, temperature gradient in the channel can be measured by the difference between maximum and minimum temperature values with an infrared camera. The

normalized steady-state temperature gradient in each channel corresponds to the eigenmode solved from the Hamiltonian. As heat transfer is inherently dissipative and it normally needs much time for the temperature field evolving into the steady state, the initial temperature gradient should be given larger (for example, 273 K for the cold-side cooling and 320 K for the hot-side heating).

To testify the topological heat funneling, we study the temperature field evolutions in a symmetric coupling structure at $a = 1$, where κ_{i0} is set to be 0.3 W m⁻¹K⁻¹. Imposing a random stimulation input, the temperature field will naturally concentrate toward the central channels, since the eigenmode of the lowest decay rate is excited and observed. In Fig. 5a, the simulated evolutions of temperature fields agree well with the tight-binding model, since the normalized temperature gradient of each channel is consistent with the theoretical analysis. However, for the asymmetric coupling case at $a = 0.4$, the temperature field tends to funnel to the designed interface at channels 10 and 11 in Fig. 5b, regardless of initial conditions. Note that the heat funneling is robust against the defects with different coupling strengths, channel numbers, and interface locations (disorder analysis can be found in Supplementary Note 3). For example, it shows the robustness when channels 2 and 3 are set with an asymmetric coupling defect ($a = 2.5$) in the model, which is different from the case in symmetric coupling systems where the temperature field localizes at the defect in Figs. 5c and 5d. The evolutions of temperature field along z axis are also presented in Figs. 5e and 5f, which validates the concept of heat funneling effect schematically displayed in Fig. 1b. Above discussions are based on the gapless system with equivalent intracell and intercell couplings. Without the loss of generality, we also investigate the gapped diffusive system with the intercell coupling much larger than asymmetric intracell couplings. In this case, the temperature field will concentrate at the channel 12, since the heat flow directions of the inverted structures change to be the same (Supplementary Note 4 and Fig. S4).

Conclusion

In summary, we investigate the physical mechanisms of diffusive skin effect and topological heat funneling. Unlike the cases in wave systems, the diffusive skin effect and heat funneling can be realized in a static framework such as directly contacted thermal metamaterials. The periodically driven Hamiltonian can be constructed in the parameter space with an aperiodic structure. Our results show that the diffusive system provides a distinctive platform to explore the topological physics and non-Hermitian dynamics. Our work is expected to inspire further exploration of other intriguing effects, including the higher-order diffusive skin effect, topological heat flow transfer, high-efficiency thermo-electric effect³⁹, heat harvesting, and thermal sensing^{40,41}, etc.

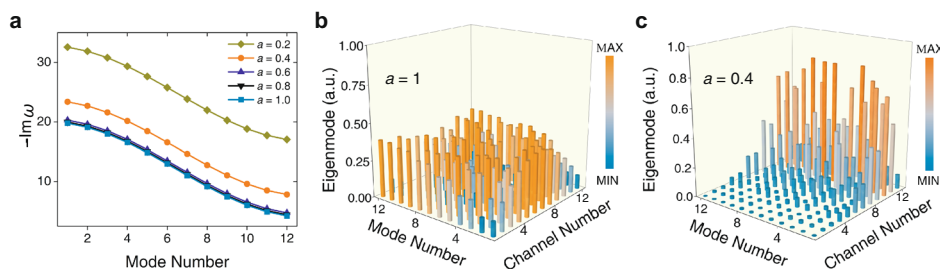


Fig. 4 Decay rates and eigenmodes. **a** Decay rates ($-\text{Im} \omega$) at different asymmetric factors a . **b** Fields of all eigenmodes with the symmetric coupling $a = 1$. **c** Fields of all eigenmodes concentrate at the interfaces with the asymmetric coupling factor $a = 0.4$.

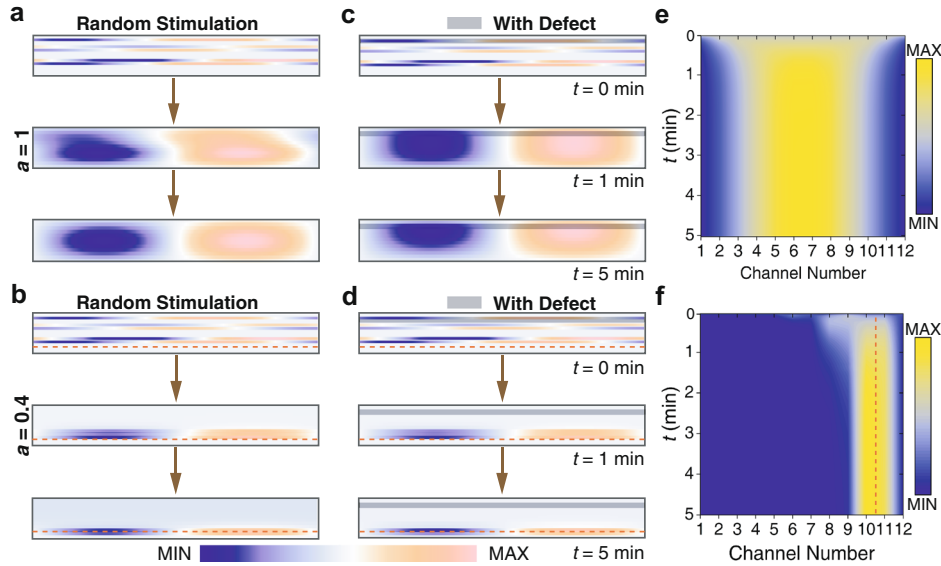


Fig. 5 Heat funneling effect. **a, b** Temperature field evolutions with time t for random stimulations at the symmetric coupling ($a = 1$) and the asymmetric coupling ($a = 0.4$), respectively. Blue color and twilight color indicate the minimum temperature and the maximum temperature. **c, d** Temperature field evolutions with an introduced asymmetric coupling defect between channels 2 and 3 for the cases in **(a)**, **(b)**. **e, f** Normalized strength evolutions of temperature intensity ($|T_{\text{grad}}|^2$) for a uniform stimulation at $a = 1$ and $a = 0.4$, where the concept of heat funneling in Fig. 1b is proved. Blue color and yellow color indicate the minimum temperature intensity and the maximum temperature intensity, respectively. The red dashed lines denote the interfaces.

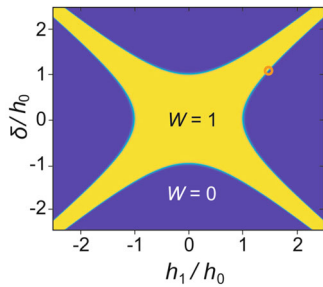


Fig. 6 Topological phase diagram. The yellow area with winding number $W = 1$ corresponds to the topological nontrivial phase, the blue area with winding number $W = 0$ corresponds to the topological trivial phase. The orange circle at the boundary denotes a phase transition point where coupling parameters $\frac{h_1}{h_0} = 1.05$ and $\frac{\delta}{h_0} = 1$.

Methods

EPs in the topological phase. As the transformation factor

$r = \sqrt{|\alpha_+ \alpha_-|} = \sqrt{\frac{h_1 + \delta}{h_1 - \delta}}$, we can deduce the Hamiltonian in OBC case to be $H_{\text{OBC}}(K + i\ln r)$. The transformed effective intracell and intercell coupling strengths are $\bar{h}_1 = \sqrt{(h_1 + \delta)(h_1 - \delta)}$ and $\bar{h}_0 = h_0$, from which we deduce $\bar{h}_1 = \bar{h}_0$. Substituting $K \rightarrow K - i\ln r$ into Eq. (4),

$$H_{\text{OBC}}(K - i\ln r) = \begin{pmatrix} iS_0 & i\frac{1}{r}(\bar{h}_1 + \bar{h}_0 e^{-iK}) \\ ir(\bar{h}_1 + \bar{h}_0 e^{iK}) & iS_0 \end{pmatrix} \quad (9)$$

The topological invariant (winding number W) is calculated by

$$W(K) = \frac{1}{2\pi i} \int_{-\pi}^{\pi} dK \frac{d}{dK} \ln \det H_{\text{OBC}}(K - i\ln r). \quad (10)$$

Figure 6 shows the topological phase diagram of the semi-infinite SSH model, where the EPs locate at the hyperbolic boundaries.

From Eq. (6) we also generate

$$|\omega - iS_0| = \sqrt{[(h_1 + \delta) + h_0 \alpha] [(h_1 - \delta) + h_0 / \alpha]}. \quad (11)$$

As $h_1 + \delta = \frac{h_0}{a}$ and $h_1 - \delta = h_0 a$, Eq. (11) can be simplified as

$$\alpha_{\pm} = \frac{1}{a} \frac{F \pm \sqrt{F^2 - 4}}{2}, \quad (12)$$

where $F = 2 - \left(\frac{\omega - iS_0}{h_0}\right)^2$. The branches of phase factors $|\alpha_{\pm}|$ coalescence are the EPs in the parameter space, with one EP at the left vertical axis and the other at $\left|\frac{\omega - iS_0}{h_0}\right| = 2$, which corresponds to the boundaries of the generalized Brillouin zone (Fig. S5 in Supplementary Note 5).

Hatano–Nelson model. The Hamiltonian of semi-infinite Hatano–Nelson model with OBC in momentum space can be expressed⁴²

$$H_{\text{HN}}(K) = iS_0 + i(h_1 + \delta)e^{-iK} + i(h_1 - \delta)e^{iK}, \quad (13)$$

and the coupling equation in real space is

$$i(h_1 + \delta)T_{n-1} + i(h_1 - \delta)T_{n+1} = (\omega_n - iS_0)T_n. \quad (14)$$

According to the diffusive non-Bloch band theory, Eq. (14) can be transformed into a standard form with phase factor $e^{iK} \rightarrow \alpha = re^{iK}$

$$i\frac{h_1 + \delta}{\alpha} + i(h_1 - \delta)\alpha = (\omega_n - iS_0). \quad (15)$$

At the zero-mode,

$$|\alpha_{\pm}| = \sqrt{\frac{h_1 + \delta}{h_1 - \delta}}. \quad (16)$$

Obviously, EPs appear at $\delta = h_1$ where the system is in absolutely asymmetric coupling. The temperature field is exponentially localized at the right boundary with the rate $|\alpha_{\pm}|$, when $0 < \delta < h_1$. In Fig. S6 (Supplementary Note 6), we show the diffusive skin effect in the Hatano–Nelson model with densities of adjacent channels and thermal capacities of interlayers having the same gradient of a^2 .

Data availability

All relevant data are available from the corresponding author X.F.Z. upon request.

Code availability

The code is available from the corresponding author X.F.Z. upon reasonable request.

Received: 3 June 2021; Accepted: 14 September 2021;

Published online: 20 October 2021

References

- Bender, C. M. & Boettcher, S. Real spectra in non-Hermitian Hamiltonians having PT symmetry. *Phys. Rev. Lett.* **80**, 5243 (1998).
- Bender, C. M. Making sense of non-Hermitian Hamiltonians. *Rep. Prog. Phys.* **70**, 947 (2007).
- El-Ganainy, R. et al. Non-Hermitian physics and PT symmetry. *Nat. Phys.* **14**, 11 (2018).
- Sounas, D. L. & Alù, A. Non-reciprocal photonics based on time modulation. *Nat. Photon* **11**, 774 (2017).
- Li, Z. P. et al. Non-Hermitian electromagnetic metasurfaces at exceptional points. *Prog. Electromagnetics Res.* **171**, 1–20 (2021).
- Zhu, X. F. et al. PT-symmetric acoustics. *Phys. Rev. X* **4**, 031042 (2014).
- Feng, L. et al. Single-mode laser by parity-time symmetry breaking. *Science* **346**, 972 (2014).
- Doppler, J. et al. Dynamically encircling an exceptional point for asymmetric mode switching. *Nature* **537**, 76 (2016).
- Liu, Q. et al. Efficient mode transfer on a compact silicon chip by encircling moving exceptional points. *Phys. Rev. Lett.* **124**, 153903 (2020).
- Chen, W. et al. Exceptional points enhance sensing in an optical microcavity. *Nature* **548**, 192 (2017).
- Assaworranit, S., Yu, X. & Fan, S. Robust wireless power transfer using a nonlinear parity–time-symmetric circuit. *Nature* **546**, 387–390 (2017).
- Wang, Q. et al. Gains maximization via impedance matching networks for wireless power transfer. *Prog. Electromagnetics Res.* **164**, 135–153 (2019).
- Coulais, C., Fleury, R. & van Wezel, J. Topology and broken Hermiticity. *Nat. Phys.* **17**, 9–13 (2020).
- Lee, T. E. Anomalous edge state in a non-Hermitian lattice. *Phys. Rev. Lett.* **116**, 133903 (2016).
- Kunst, F. K., Edvardsson, E., Budich, J. C. & Bergholtz, E. J. Biorthogonal bulk-boundary correspondence in non-Hermitian systems. *Phys. Rev. Lett.* **121**, 26808 (2018).
- Yao, S. & Wang, Z. Edge states and topological invariants of non-Hermitian systems. *Phys. Rev. Lett.* **121**, 86803 (2018).
- Yao, S., Song, F. & Wang, Z. Non-Hermitian Chern bands. *Phys. Rev. Lett.* **121**, 136802 (2018).
- Yokomizo, K. & Murakami, S. Non-Bloch band theory of non-Hermitian systems. *Phys. Rev. Lett.* **123**, 66404 (2019).
- Kawabata, K., Shiozaki, K., Ueda, M. & Sato, M. Symmetry and topology in non-Hermitian physics. *Phys. Rev. X* **9**, 41015 (2019).
- Okuma, N., Kawabata, K., Shiozaki, K. & Sato, M. Topological origin of non-Hermitian skin effects. *Phys. Rev. Lett.* **124**, 86801 (2020).
- Shan, Q., Yu, D., Li, G., Yuan, L. & Chen, X. One-way topological states along vague boundaries in synthetic frequency dimensions including group velocity dispersion. *Prog. Electromagnetics Res.* **169**, 33–43 (2020).
- Li, L., Lee, C. & Gong, J. Impurity induced scale-free localization. *Commun. Phys.* **4**, 42 (2021).
- Weidemann, S. et al. Topological funneling of light. *Science* **368**, 311 (2020).
- Ghatak, A., Brandenbourger, M., Wezel, J. V. & Coulais, C. Observation of non-Hermitian topology and its bulk-edge correspondence in an active mechanical metamaterial. *Proc. Natl Acad. Sci. U.S.A.* **47**, 29561 (2020).
- Xiao, L. et al. Non-Hermitian bulk-boundary correspondence in quantum dynamics. *Nat. Phys.* **16**, 761 (2020).
- Helbig, T. et al. Generalized bulk-boundary correspondence in non-Hermitian topoelectrical circuits. *Nat. Phys.* **16**, 747 (2020).
- Yang, S. et al. Controlling macroscopic heat transfer with thermal metamaterials: theory, experiment and application. *Phys. Rep.* **908**, 1–65 (2021).
- Li, Y. et al. Transforming heat transfer with thermal metamaterials and devices. *Nat. Rev. Mater.* **6**, 488–507 (2021).
- Fan, C. Z., Gao, Y. & Huang, J. P. Shaped graded materials with an apparent negative thermal conductivity. *Appl. Phys. Lett.* **92**, 251907 (2008).
- Shen, X., Jiang, C., Li, Y. & Huang, J. P. Thermal metamaterial for convergent transfer of conductive heat with high efficiency. *Appl. Phys. Lett.* **109**, 201906 (2016).
- Peng, Y. G. et al. 3D printed meta-helmet for wide-angle thermal camouflages. *Adv. Funct. Mater.* **30**, 2002061 (2020).
- Guenneau, S., Amra, C. & Veynante, D. Transformation thermodynamics: cloaking and concentrating heat flux. *Opt. Express* **20**, 8207 (2012).
- Li, Y. et al. Temperature-dependent transformation thermotics: from switchable thermal cloaks to macroscopic thermal diodes. *Phys. Rev. Lett.* **115**, 195503 (2015).
- Li, Y., Li, J., Qi, M., Qiu, C.-W. & Chen, H. Diffusive nonreciprocity and thermal diode. *Phys. Rev. B* **103**, 014307 (2021).
- Li, Y. & Li, J. Advection and thermal diode. *Chin. Phys. Lett.* **38**, 030501 (2021).
- Li, Y. et al. Anti-parity-time symmetry in diffusive systems. *Science* **364**, 170 (2019).
- Xu, L., Dai, G., Wang, G. & Huang, J. Geometric phase and bilayer cloak in macroscopic particle-diffusion systems. *Phys. Rev. E* **102**, 32140 (2020).
- Cao, P. et al. High-order exceptional points in diffusive systems: robust APT symmetry against perturbation and phase oscillation at APT symmetry breaking. *ES Energy Environ.* **7**, 48 (2020).
- Xu, Y., Gan, Z. & Zhang, S. Enhanced thermoelectric performance and anomalous Seebeck effects in topological insulators. *Phys. Rev. Lett.* **112**, 226801 (2014).
- Budich, J. C. & Bergholtz, E. J. Non-Hermitian topological sensors. *Phys. Rev. Lett.* **125**, 180403 (2020).
- Xu, H. et al. A combined active and passive method for the remote sensing of ice sheet temperature profiles. *Prog. Electromagnetics Res.* **167**, 111–126 (2020).
- Hatano, N. & Nelson, D. R. Localization transitions in non-Hermitian quantum mechanics. *Phys. Rev. Lett.* **77**, 570 (1996).

Acknowledgements

We thank Prof. Baowen Li for the useful suggestions and discussions. This work was supported by National Natural Science Foundation of China (Grant Nos. 11690030, 11690032 and 92163123).

Author contributions

P.C.C., Y.L. and X.F.Z. conceptualized this work and carried out the theoretical modeling, simulations and data analyses. Y.G.P., M.Q., W.X.H. and P.Q.L. provided useful suggestions. X.F.Z. and Y.L. supervised this project. All authors wrote the paper.

Competing interests

The authors declare no competing interests.

Additional information

Supplementary information The online version contains supplementary material available at <https://doi.org/10.1038/s42005-021-00731-z>.

Correspondence and requests for materials should be addressed to Ying Li or Xue-Feng Zhu.

Peer review information *Communications Physics* thanks the anonymous reviewers for their contribution to the peer review of this work. Peer reviewer reports are available.

Reprints and permission information is available at <http://www.nature.com/reprints>

Publisher's note Springer Nature remains neutral with regard to jurisdictional claims in published maps and institutional affiliations.



Open Access This article is licensed under a Creative Commons Attribution 4.0 International License, which permits use, sharing, adaptation, distribution and reproduction in any medium or format, as long as you give appropriate credit to the original author(s) and the source, provide a link to the Creative Commons license, and indicate if changes were made. The images or other third party material in this article are included in the article's Creative Commons license, unless indicated otherwise in a credit line to the material. If material is not included in the article's Creative Commons license and your intended use is not permitted by statutory regulation or exceeds the permitted use, you will need to obtain permission directly from the copyright holder. To view a copy of this license, visit <http://creativecommons.org/licenses/by/4.0/>.

© The Author(s) 2021